Interfacial patterns in magnetorheological fluids: Azimuthal field-induced structures

Eduardo O. Dias,[1,*] Sérgio A. Lira,[2,†] and José A. Miranda[1,‡]
[1]*Departamento de Física, Universidade Federal de Pernambuco, Recife, Pernambuco 50670-901 Brazil*
[2]*Instituto de Física, Universidade Federal de Alagoas, Maceió, Alagoas 57072-900 Brazil*
(Received 26 May 2015; published 4 August 2015)

Despite their practical and academic relevance, studies of interfacial pattern formation in confined magnetorheological (MR) fluids have been largely overlooked in the literature. In this work, we present a contribution to this soft matter research topic and investigate the emergence of interfacial instabilities when an inviscid, initially circular bubble of a Newtonian fluid is surrounded by a MR fluid in a Hele-Shaw cell apparatus. An externally applied, in-plane azimuthal magnetic field produced by a current-carrying wire induces interfacial disturbances at the two-fluid interface, and pattern-forming structures arise. Linear stability analysis, weakly nonlinear theory, and a vortex sheet approach are used to access early linear and intermediate nonlinear time regimes, as well as to determine stationary interfacial shapes at fully nonlinear stages.

DOI: 10.1103/PhysRevE.92.023003 PACS number(s): 47.54.−r, 47.65.Cb, 83.80.Gv, 47.15.gp

I. INTRODUCTION

Magnetorheological (MR) fluids [1–5] are suspensions of micrometersized magnetic particles in a nonmagnetic carrier fluid. The particles are multidomain and only produce a net magnetization when an external magnetic field is applied. Under the influence of an external magnetic field the suspension undergoes a structural transition in such a way that the randomly dispersed particles tend to aggregate and arrange themselves to form long chains, columns, and even intricate networks. This responsive behavior leads to a rheological change of MR fluids from a liquid to a solidlike state, which occurs quite rapidly and is of reversible nature. Therefore, MR fluids are markedly non-Newtonian, presenting a distinguishing magnetic field-dependent yield stress. Yield-stress fluids are characterized by the fact that they can sustain finite stress without flow [6–9].

Although research on MR fluids was originally initiated in 1948 [1], it was only in the early 1990s they were rediscovered when the "smart fluids" started to be used to produce a massive number of technological devices [10]. Because of their peculiar properties, MR fluids provide an efficient way to design simple and fast electromechanical systems [11,12]. A number of important technological applications range from the development of smart suspension damping in the automotive industry, vibration control in washing machines, and earthquake vibration control in buildings, through grinding and polishing applications [13,14]. Another relevant topic, of both scholarly and practical interest, addresses the possibility of using MR fluids to produce magnetic field-controllable adhesion to nonmagnetic surfaces [15–17]. This novel MR fluid-based form of controllable adhesion can potentially be applied to motion control in robotics [18,19].

At this point we briefly comment on a different kind of magnetic fluid, named *ferrofluid* [20,21], that has also attracted much attention from physicists, chemists, and engineers since the early 1960s. Ferrofluids present constitutive and flow properties that are very distinct from those disclosed by MR fluids [22,23]. For instance, instead of being composed by multidomain, micronsized magnetic grains, the particles in ferrofluids consist of monodomain, nanometersized structures. In ferrofluids Brownian motion (thermal fluctuations) prevents particles from settling under gravity, while in MR fluids particles are too heavy for Brownian motion to keep them suspended and thus can eventually settle over time. Another key difference between ferrofluids and MR fluids is related to chaining phenomena: While MR fluids chain easily under the action of an external magnetic field, ferrofluids normally show no tendency toward chain formation. These differing features make ferrofluids typically Newtonian, while MR fluids are notably non-Newtonian, yield stress fluids.

Despite the fact that MR fluids have been extensively studied (both experimentally and theoretically) since the mid-1990s [1–5,10–19], relatively limited attention has been given to the study of interfacial pattern formation in these soft matter materials. This stands in contrast to what happens in the research of ferrofluids, where interfacial pattern formation has been vastly investigated [24]. This is particularly true for the case of confined ferrofluids, where a viscous ferrofluid droplet is surrounded by a nonmagnetic fluid and placed in the narrow (effectively two-dimensional) space between two parallel glass plates of a Hele-Shaw cell [25–35]. Depending on the nature and symmetry properties of the applied magnetic field a variety of interfacial patterned morphologies can be obtained: If the applied magnetic field is uniform and perpendicular to the Hele-Shaw cell plates, then it destabilizes the ferrofluid interface and one observes the formation of highly convoluted, multiply branched, labyrinthine patterns [25–29]. If the applied field increases radially and is applied in the plane of the Hele-Shaw cell, it is also destabilizing, and the development of interesting polygon-shaped and starfishlike ferrofluid patterns is verified [30,31]. Likewise, if the applied field is an in-plane ac rotating magnetic field, then it deforms the ferrofluid droplet, and the formation of amazing spiral shapes is unveiled [32]. However, if one uses the in-plane azimuthal magnetic field generated by a current-carrying wire, it tends to stabilize the ferrofluid interface. This azimuthal field stabilizing scheme has been proven effective to control interfacial instabilities in ferrofluids under centrifugally

*eduardodias@df.ufpe.br
†sergio@fis.ufal.br
‡jme@df.ufpe.br

induced fingering in rotating Hele-Shaw cells [33–35], resulting in the emergence of interesting diamond-ring-shaped patterns.

As indicated earlier, pattern formation studies of confined MR fluids are quite scarce in the literature. There are only a few isolated examples: The experimental investigation performed in Ref. [36] used a MR fluid to control both the amplitude and wavelength of the initial perturbations arising in the Rayleigh-Taylor instability problem. A couple of other theoretical studies examined the growth of interfacial patterns when an initially circular drop of MR fluid is encircled by a nonmagnetic inviscid fluid: (i) first, when the system is subjected to a stabilizing azimuthal magnetic field in a rotating Hele-Shaw cell [35], and then (ii) when a destabilizing radial field acts in the usual motionless Hele-Shaw cell arrangement [37]. These last two investigations [35,37] have demonstrated that the resulting MR fluid interfacial patterns significantly differ from the equivalent structures generated when a ferrofluid is utilized [30,34]. This reinforces the idea that there is plenty of room to study still unexplored pattern morphologies and novel dynamical behaviors of magnetic field-induced MR fluid structures in the Hele-Shaw setup.

In this work we consider an additional field-induced, pattern-forming system recently proposed in the ferrofluid literature [38] and extend it to the realm of the MR fluid research. Reference [38] reported a theoretical treatment of the interfacial instabilities in a Hele-Shaw cell containing an initially circular bubble of an inviscid nonmagnetic fluid surrounded by a ferrofluid. Under such circumstances (magnetic fluid is the outer fluid), the interface becomes *unstable* due to the action of an in-plane azimuthal magnetic field produced by a current-carrying wire placed normal to the cell plates. This situation contrasts to previous azimuthal field studies [33–35] in which the ferrofluid was the inner fluid, so the azimuthal field acted to stabilize the interface. As a result of such study [38] innovative nonlinear interface responses and uncommon pattern-forming shapes have been identified.

Here we revisit the destabilizing azimuthal magnetic field setup proposed in Ref. [38] but now consider that the outer fluid is a MR fluid. Motivated by the fact that MR fluids (non-Newtonian suspensions of micrometersized magnetic particles) are quite distinct from ferrofluids (Newtonian colloid of nanometersized magnetic particles), and by knowing that these two types of magnetic fluids respond very differently to external applied fields, we try to access new aspects of the pattern forming dynamics. Additionally, we search for still-unexploited MR fluid interfacial pattern conformations. Linear stability analysis, weakly nonlinear theory, and a fully nonlinear vortex sheet formalism are employed to gain analytical and numerical insight into the fluid-fluid interface time evolution and into the establishment of stationary MR fluid patterns.

II. LINEAR AND WEAKLY NONLINEAR ANALYSES

A. Dynamics of interfacial perturbations

In this section, our main goal is to describe analytically and perturbatively the time evolution of the interface separating a nonmagnetic, inviscid inner fluid, and an outer MR fluid,

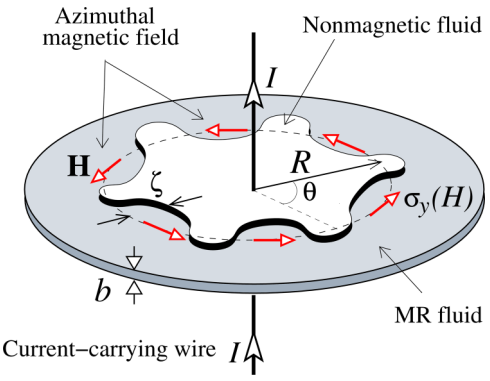

FIG. 1. (Color online) Representative sketch of a Hele-Shaw cell setup containing an inviscid nonmagnetic fluid bubble surrounded by a viscous MR fluid of magnetic field-dependent yield stress $\sigma_y(H)$. The in-plane azimuthal magnetic field $\mathbf{H}$ is produced by a long wire carrying an electric current I.

considering that they are confined in a Hele-Shaw cell of thickness b (Fig. 1). The MR fluid obeys a Bingham rheological law with yield stress [see Eq. (2)], presenting a constant plastic viscosity η. The surface tension at the fluid-fluid interface is denoted by γ. The interface destabilization is induced by the action of an azimuthal magnetic field $\mathbf{H}$ produced by a current-carrying wire,

$$\mathbf{H} = \frac{I}{2\pi r}\hat{\mathbf{e}}_\theta, \tag{1}$$

that is perpendicular to (coaxial with) the plates of the Hele-Shaw cell. A magnetic body force $\sim\nabla H$, where $H = |\mathbf{H}|$ is the local magnetic field intensity, acts on the MR fluid pointing in the inward radial direction [20,38]. Since the applied magnetic field presents a natural nonzero gradient, we take it as the main local field contribution to the magnetic body force. In our analysis we have not considered the influence of the demagnetizing (or induction) field [20,21]. In the Appendix we present a discussion about the role played by demagnetizing effects and show that within the scope of our problem they can be safely neglected. Stabilization of the system is provided by surface tension and yield stress effects. The electric current is represented by I, r is the radial distance from the origin of the coordinate system (located at the center of the cell), and $\hat{\mathbf{e}}_\theta$ is a unit vector in the azimuthal direction.

In this framing, we examine the early time (purely linear) stage of the flow, as well as the intermediate time (weakly nonlinear) regime, during which important nonlinear effects start to become relevant. In order to do that, we employ a perturbative mode-coupling approach that enables one to derive a differential equation describing the time evolution of the interfacial perturbation amplitudes. Within the scope of our second-order mode-coupling theory [39] the perturbed shape of the interface can be written as $\mathcal{R}(\theta,t) = R + \zeta(\theta,t)$, where R is the radius of the initially circular two-fluid interface and θ is the azimuthal angle (see Fig. 1). Here $\zeta(\theta,t) = \sum_{n=-\infty}^{+\infty} \zeta_n(t)\exp(in\theta)$ represents the net interface perturbation with complex Fourier amplitudes $\zeta_n(t)$ and discrete azimuthal wave numbers n.

One of the most relevant rheological properties of a MR fluid is the existence of a magnetic field-dependent yield

stress. We follow Refs. [3–5,16,17,35] and write a constitutive equation relating shear yield stress to external magnetic field strength as

$$\sigma_y(H) = \sigma_{y0} + \alpha H^2, \tag{2}$$

where σ_{y0} represents a small yield stress present even in the absence of the magnetic field, and α is a constant that depends on the material properties of the MR fluid, being proportional to the particle volume fraction [5].

Since we are interested in examining an interface destabilization process, in deriving the governing equation (3) we consider the regime of high viscosity compared to yield effects, where flow is facilitated. This is known as the small Bingham number limit (Bi < 0.2) [40], where Bi measures the ratio between yield stress and viscous effects. In addition, as the magnetic body force induced by the azimuthal field points radially inward [20,33], we take the prevalent yielding occurring along the radial direction. Under such conditions, the effectively two-dimensional dynamics of the system can be described by a modified Darcy's law for the gap-averaged velocity [16,17,40,41],

$$\mathbf{v} = -\frac{b^2}{12\eta}\left[\nabla\Pi - \frac{3\sigma_y(H)}{b}\hat{\mathbf{e}}_r\right], \tag{3}$$

where $\hat{\mathbf{e}}_r$ denotes the unit vector along the radial direction. In Eq. (3) the gap-averaged generalized pressure is defined as [26]

$$\Pi = \frac{1}{b}\int_{-b/2}^{+b/2}[P - \Psi]dz, \tag{4}$$

where P is the three-dimensional pressure,

$$\Psi = \mu_0\int_0^H M dH = \frac{\mu_0\chi H^2}{2} \tag{5}$$

represents a magnetic pressure [20,33], and μ_0 denotes the magnetic permeability of free space. In Eq. (5) we used the linear relationship $\mathbf{M} = \chi\mathbf{H}$, with $M = |\mathbf{M}|$ being the magnetization of the MR fluid and χ its magnetic susceptibility.

Before we continue, we call the readers' attention to the fact that MR fluids are indeed complex anisotropic media, possessing anisotropic magnetic and rheological properties [1–5]. With this in mind, we stress that our current analysis applies to homogeneous isotropic media. In this context, our simplified theoretical approach allows us to capture the qualitative features of the interfacial instability occurring in real MR fluids. To support our homogeneity assumption for the MR fluid, at the end of this section we provide a comparative estimation of the characteristic times of particle migration (τ_m) and instability development (τ_i).

Since the yield term [second term in brackets of Eq. (3)] can be expressed as a gradient of some scalar function, the velocity field is irrotational in the bulk, and we can state our problem in terms of a velocity potential ϕ, where $\mathbf{v} = -\nabla\phi$. Moreover, from the incompressibility condition $\nabla\cdot\mathbf{v} = 0$ it can be seen that the velocity potential is indeed Laplacian, so we have that $\nabla^2\phi = 0$. At first glance, it may seem very simple to solve this Laplace equation. The basic equations for this system are actually simple. However, their solutions are definitely not so simple. The difficulty of solving the Laplace's equation lies in the existence of moving boundary conditions, which involve a functional of the unknown interface shape. This is what is called a free boundary problem, which is in general not possible to be solved analytically in a close form. However, as we will verify throughout this work, tackling the problem via an analytical perturbative approach is quite feasible and reveals valuable insights regarding the linear and weakly nonlinear dynamics of the system.

In the context of Hele-Shaw flows [42], our Laplacian problem is specified by two boundary conditions. The first one is the augmented pressure jump boundary condition [20,21],

$$p|_{r=\mathcal{R}} = -\left[\gamma\kappa + \frac{1}{2}\mu_0(\mathbf{M}\cdot\hat{\mathbf{n}})^2\right]_{r=\mathcal{R}}, \tag{6}$$

where $p = [\int_{-b/2}^{+b/2} P dz]/b$ and $\hat{\mathbf{n}}$ denotes the unit normal vector at the interface. The first term on the right-hand side of Eq. (6) expresses the conventional contribution related to surface tension and interfacial curvature κ. The second term on the right-hand side of (6) is related to the magnetic nature of the problem: It is commonly known as the magnetic normal traction term [20,21,35] and incorporates the influence of the discontinuous normal component of the magnetization at the interface. This particular magnetic contribution has a key role in determining the shape of the emergent MR fluid interfacial patterns. The remaining boundary condition (commonly known as the kinematic boundary condition [42]) connects the velocity of the MR fluid with the motion of the interface itself,

$$\frac{\partial\mathcal{R}}{\partial t} = \left[\frac{1}{r^2}\frac{\partial\mathcal{R}}{\partial\theta}\frac{\partial\phi}{\partial\theta} - \frac{\partial\phi}{\partial r}\right]_{r=\mathcal{R}}. \tag{7}$$

Equation (7) expresses the fact that the normal components of the fluids velocities are continuous across the interface.

To complete our derivation we define Fourier expansions for the velocity potential and use the kinematic boundary condition (7) to express the Fourier coefficients of ϕ in terms of ζ_n. Substituting these relations and the pressure jump condition (6) into a modified Darcy's law [Eq. (3)], always keeping terms up to second order in ζ and Fourier transforming, we find the *dimensionless* equation of motion for the perturbation amplitudes ζ_n (for $n \neq 0$). We present the evolution of the perturbation amplitudes in terms of the k-th order in the perturbation ($k = 1, 2$)

$$\dot{\zeta}_n = \dot{\zeta}_n^{(1)} + \dot{\zeta}_n^{(2)}, \tag{8}$$

with

$$\dot{\zeta}_n^{(1)} = \lambda(n)\zeta_n, \tag{9}$$

where the overdot represents a total time derivative with respect to time,

$$\lambda(n) = |n|\left[\frac{\chi N_B}{R^4} - \frac{(n^2-1)}{R^3} - \frac{S_0}{R} - \frac{S}{R^3}\right] \tag{10}$$

denotes the linear growth rate, and

$$\dot{\zeta}_n^{(2)} = \sum_{n'\neq 0}[F(n,n')\zeta_{n'}\zeta_{n-n'} + G(n,n')\dot{\zeta}_{n'}\zeta_{n-n'}]. \tag{11}$$

The functions $F(n,n')$ and $G(n,n')$ are the second-order mode-coupling terms given by

$$F(n,n') = -\frac{|n|}{R}\left\{\frac{3}{2}\chi\frac{N_B}{R^4}\left[1+\frac{1}{3}\chi n'(n'-n)\right] + \frac{1}{R^3}\left[1-\frac{n'}{2}(3n'+n)\right] - \frac{S}{R^3}\right\}, \quad (12)$$

and

$$G(n,n') = \frac{1}{R}\{|n|[1-\mathrm{sgn}(nn')]-1\}. \quad (13)$$

In Eq. (13) the sign function sgn equals ± 1 according to the sign of its argument. In Eqs. (8)–(13) lengths and time are rescaled by r_0 and $(12\eta r_0^3)/(b^2\gamma)$, respectively, where r_0 is a typical length being on the order of the unperturbed droplet radius R. Note that, in the remainder of this paper, we work with the dimensionless version of the equations. Within this dimensionless description the system is conveniently characterized by three governing parameters,

$$N_B = \frac{\mu_0 I^2}{4\pi^2\gamma r_0}, \quad S_0 = \frac{3\sigma_{y0} r_0^2}{\gamma b}, \quad \text{and} \quad S = \frac{3\alpha I^2}{4\pi^2\gamma b}.$$

The parameter N_B represents the magnetic Bond number and measures the ratio of magnetic to capillary forces. On the other hand, S_0 and S are related to the yield-stress contributions at zero and nonzero applied magnetic field, respectively. We emphasize that in the presentation of our results in the next sections we make sure that the values of all relevant dimensionless quantities we utilize are consistent with realistic physical parameters [17,35,37,43–45] related to existing magnetic field arrangements and material properties of MR fluids. The condition of validity for our model presented at the beginning of Sec. II A can be written as $\mathrm{Bi} = (b\sigma_{y0})/(\eta\dot{\zeta}) < 0.2$. We have verified that such a condition holds for the range of parameters used in our problem.

As commented earlier in this section, here we substantiate our homogeneity assumption for the MR fluid. We do that by comparing the characteristic migration time of the magnetic particles induced by the field gradient, with the typical time scale for instability development. In Ref. [46] (see p. 1835) this migration time is calculated by taking into consideration magnetic forces and hydrodynamic drag acting on the magnetic particles. Applying their expression for the migration time to our problem, we obtain

$$\tau_m = \frac{3\eta r_0^2}{2\mu_0[H(r_0)]^2 a_0^2} \sim 10^7 \text{ s}, \quad (14)$$

where the particle radius $a_0 \approx 1$ μm, $\eta = 0.1$ Pa s, $r_0 \approx 10^{-2}$ m, $H \approx 1$ kA/m, and $\mu_0 = 4\pi \times 10^{-7}$ Tm/A. On the other hand, the typical time for instability development in our problem is

$$\tau_i = \frac{12\eta r_0^3}{b^2\gamma} \sim 10^2 \text{ s}, \quad (15)$$

where $b \approx 10^{-4}$ m and $\gamma = 0.3$ N/m. It is clear that $\tau_m \gg \tau_i$, indicating that the effect of particle migration on our interfacial instability problem can be neglected. This supports our assumption that the MR fluid can be considered as a homogeneous medium.

B. Discussion: Linear and weakly nonlinear regimes

By inspecting Eq. (10) for the linear growth rate, one readily notices that it is a time-independent quantity. Therefore, at the linear level, Eq. (9) can be easily integrated, resulting in the exponential growth (decay) of the linear perturbation amplitudes with time if $\lambda(n) > 0$ [$\lambda(n) < 0$]. In this context, it is also clear that the only destabilizing term in Eq. (10) is the one related to the azimuthal magnetic field (term proportional to N_B). On the other hand, the contribution coming from surface tension [term proportional to (n^2-1)], and yield stress (both S_0 and S) effects act to restrain interface deformation. A quantity of interest that can be extracted from the linear growth rate is the critical value of the magnetic Bond number at which the n-th mode becomes unstable. This happens when $\lambda(n) = 0$ and is given by

$$N_B^{\mathrm{crit}}(n) = \frac{R}{\chi}[(n^2-1) - R^2 S_0 - S]. \quad (16)$$

From this expression we realize that the minimum value of $N_B^{\mathrm{crit}}(n)$ required to drive the system unstable occurs when $n = 2$. These are essentially the most important pieces of information that can be extracted at a purely linear level (i.e., *stability* behavior of the circular interface against small perturbations).

Now we turn our attention to the mode-coupling, second-order contributions expressed in Eq. (11). The terms appearing in the expression for the function $F(n,n')$ in Eq. (12) arise from the magnetic applied field, surface tension, and field-dependent yield stress, respectively. The term proportional to χ^2 comes from the square of the projection of the interface normal in the azimuthal direction in the pressure jump condition [Eq. (6)]. In addition, the function $G(n,n')$ defined in Eq. (13) couples the perturbed flow $\dot{\zeta}$ with the interface shape perturbation ζ and presents no dependence on magnetic effects.

An important aspect of our second-order perturbative approach is the fact that, through the coupling of just a few Fourier modes, one is able to extract key analytical information about the *morphology* of the interface (shape of the fingering structures) at the onset of nonlinearities [39]. From Eq. (9) it is evident that, at the linear level, the participating Fourier modes do not couple, so a mode n does not affect the dynamical evolution of a mode n'. However, at second order in ζ, the situation considerably differs: From Eq. (11) one can verify that the time evolution of a given mode n is actually influenced by an infinite number of modes n'. In this sense a second-order multimode perturbative analysis should imply the solution of a complicated set of coupled, nonlinear differential equations. Depending on the number of interacting modes one wishes to take into account, the analytical assessment of the interfacial pattern evolution can be considerably challenging. Fortunately, it is possible to circumvent this difficulty in such a way that a description of the underlying nonlinear pattern forming mechanisms can still be captured by considering the interplay of a few participating Fourier modes.

In fact, Miranda and Widom [39] have shown that a weakly nonlinear, mode-coupling analysis based on Eq. (8) is quite effective in providing very useful clues about the typical shapes of the emerging fingering structures in Hele-Shaw cell problems. For instance, in order to find out if a given

interfacial finger would tend to be wide or narrow, it has been shown that one does not need to consider the complicated coupling of an infinite (or a large) number of Fourier modes, but just to examine the interaction of two specific modes: namely a fundamental mode and its associated first harmonic. In this way, the basic morphological mechanism of fingertip widening or fingertip narrowing could be efficiently captured even at the lowest nonlinear order and by considering the interplay between just two Fourier modes. The effectiveness of this particular weakly nonlinear strategy has been amply substantiated by a number of analytical, numerical, and experimental studies in the Hele-Shaw flow literature (see, for instance, Refs. [47–55]).

To investigate the shape of the uprising MR fluid fingering structures at the weakly nonlinear regime, we follow Ref. [39]. We begin our analysis by rewriting Eq. (8) in terms of cosine and sine modes, where the cosine $a_n = \zeta_n + \zeta_{-n}$ and sine $b_n = i(\zeta_n - \zeta_{-n})$ amplitudes are real valued. As in Ref. [39] we choose the phase of the fundamental mode so $a_n > 0$ and $b_n = 0$. As pointed out earlier, within the scope of our mode-coupling description, fingertip widening, and fingertip narrowing can be described by considering the influence of a fundamental mode n on the growth of its first harmonic $2n$. Writing the equations of motion for the harmonic mode we have

$$\dot{a}_{2n} = \lambda(2n)a_{2n} + \tfrac{1}{2}T(2n,n)a_n^2, \tag{17}$$

$$\dot{b}_{2n} = \lambda(2n)b_{2n}, \tag{18}$$

where the fingertip function is defined as

$$T(2n,n) = F(2n,n) + \lambda(n)G(2n,n). \tag{19}$$

Since the growth of the sine mode b_{2n} is uninfluenced by a_n and does not present second-order couplings, we focus on the growth of the cosine mode a_{2n} which is given by Eq. (17).

Even without explicitly solving Eq. (17), just by inspection one can assess valuable information about possible shapes assumed by the emergent interfacial fingers. It is known that the function $T(2n,n)$ dictates the fingertip behavior [30,39]. From Eq. (17), notice that, depending on the sign of $T(2n,n)$, the term of order a_n^2 can drive the growth of a_{2n} either positively or negatively. If $T(2n,n) < 0$, a_n^2 is driven negatively, making that the inward pointing fingers of the MR fluid will tend to be narrow at their tips. In this case $[T(2n,n) < 0]$, the outward-pointing fingers of the nonmagnetic bubble would have blunt tips.

Reversing the sign of $T(2n,n)$ exactly reverses the above conclusions. If the fingertip function is positive, a_n^2 is driven positively, a phase that results in MR fluid inward-pointing fingers that become wide and flat at their tips. In this situation $[T(2n,n) > 0]$, the outward-pointing fingers of the bubble are the ones that tend to be comparatively narrower.

To begin extracting the most relevant morphological features of the emerging fingering patterns by using the weakly nonlinear approach, in Fig. 2 we plot $T(2n,n)$ as a function of the Fourier mode n for two values of magnetic Bond number N_B: 15 and 25. It is also illustrated how the fingertip function behaves when the magnetic field-dependent yield stress parameter S is modified: the solid (dashed) curve considers that $S = 10$ $(S = 2)$. Here we fixed $\chi = 1$ and $S_0 = 0.5$.

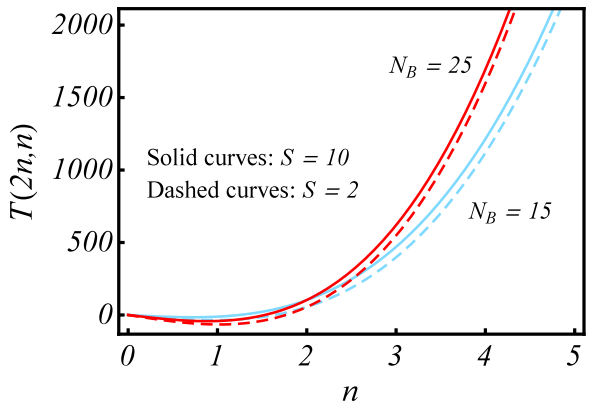

FIG. 2. (Color online) Behavior of the fingertip function $T(2n,n)$ as the Fourier mode n is varied for $N_B = 15$ and $N_B = 25$. Solid (dashed) curves represent the situation for the magnetic field-dependent yield stress parameter $S = 10$ $(S = 2)$.

By examining Fig. 2, we verify that the fingertip function $T(2n,n)$ is positive for $n \geqslant 2$ and that it grows quickly as the value of n is increased. This indicates that the nonlinear effects favor the development of inward-pointing fingers of the MR fluid presenting wide tips. Additionally, one can see that such a fingertip-widening behavior becomes more intense for larger values of N_B. It is also worth noting that, since the solid curves are located above the dashed ones, larger values of S lead to enhanced fingertip broadening of the MR fluid inward-pointing structures. Finally, as indicated previously in this section, all these findings also anticipate the simultaneous formation of outward-pointing fingering structures of the nonmagnetic bubble that are narrower at their tips, as compared to the corresponding inward-pointing fingers of the MR fluid.

In order to reinforce and better illustrate the major conclusions obtained from the analysis of Fig. 2, in Fig. 3 we plot the time evolution of the interface considering the interaction of two representative cosine modes, a fundamental mode n, and its first harmonic $2n$. In each pattern depicted in Fig. 3 eight snapshots of the evolving interface are shown, separated at equal time intervals, for three different values of N_B: (a) $N_B = 25$, $n = 3$, and $0 \leqslant t \leqslant 0.4$; (b) $N_B = 35$, $n = 4$, and $0 \leqslant t \leqslant 0.4$; and (c) $N_B = 50$, $n = 5$, and $0 \leqslant t \leqslant 0.28$. The thicker black interface is the one obtained at the final time. The fundamental mode was chosen as being the highest mode inside the linear instability band [defined by setting $\lambda(n) = 0$] so the first harmonic dynamics is driven by just nonlinear effects. In addition, we keep fixed $\chi = 0.65$, $S_0 = 1$, and $S = 2$. The initial perturbation amplitudes are taken as $a_n(0) = 10^{-3}$ and $a_{2n}(0) = 5 \times 10^{-4}$.

By observing Fig. 3, we see the formation of N-fold interfacial patterns with $N = 3$, 4, and 5 presenting inward pointing fingers of the MR fluid that tend to grow wide and flat at their tips. As predicted by the fingertip function analysis (Fig. 2), these blunt fingering structures of the MR fluid are accompanied by outward-pointing fingers of the nonmagnetic inner bubble that are evidently narrower at their tips.

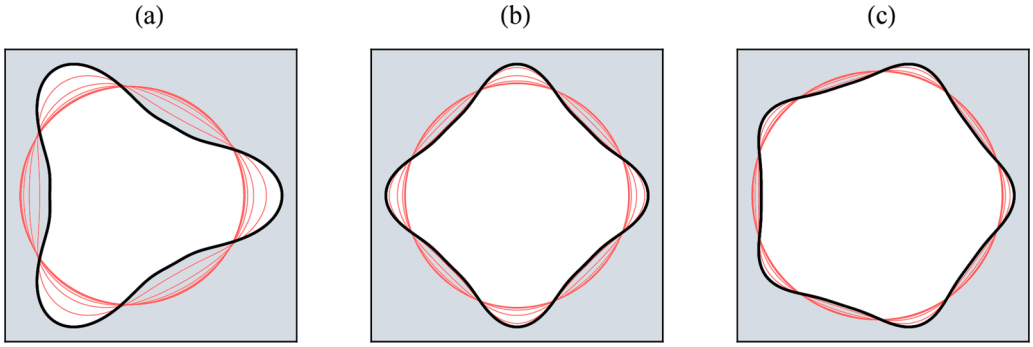

FIG. 3. (Color online) Snapshots of the evolving interface, showed at equal time intervals for the interaction of two cosine modes. The values of N_B increase from left to right, and three different fundamental modes are considered: (a) $N_B = 25$, $n = 3$, and $0 \leqslant t \leqslant 0.4$; (b) $N_B = 35$, $n = 4$, and $0 \leqslant t \leqslant 0.4$; and (c) $N_B = 50$, $n = 5$, and $0 \leqslant t \leqslant 0.28$. The thicker solid black curve represents the final time interface. All depicted N-fold patterns ($N = 3$,4, and 5) present the formation of wide, flat penetrating fingers of the MR fluid. The outward moving fingers of the nonmagnetic bubble are clearly narrower at their tips.

III. FULLY NONLINEAR STEADY SHAPES

In the previous section we have seen that linear stability analysis provides useful information about the stability of the interface separating the nonmagnetic and the MR fluid at initial stages of the dynamics. Furthermore, we have also verified that a second-order weakly nonlinear theory is able to extract important information about the morphology of the fingering patterns at intermediate time regimes. In this section, however, our main purpose is to have access to fully nonlinear features of the pattern formation process in a *nonperturbative* fashion. One useful method utilized to accomplish this task in the Hele-Shaw setup is a technique known as the vortex sheet approach [56,57].

As mentioned in Sec. II A the kinematic boundary condition (7) expresses the fact that the normal component of the fluids velocities are continuous when one crosses the two-fluid interface [42]. In contrast, the tangential components of the velocities are discontinuous across the interface and give rise to a region of nonzero vorticity. Therefore, Hele-Shaw flows are assumed to be irrotational, except right at the interface.

The vortex sheet formalism explores the jump in the tangential component of the fluid velocity and defines the vortex sheet strength as

$$\Gamma = (\mathbf{v}_1 - \mathbf{v}_2)\cdot\hat{\mathbf{s}}, \tag{20}$$

where $\mathbf{v}_1$ and $\mathbf{v}_2$ are the two limiting values (from the outer and inner sides of the interface, respectively) of the velocity at a given point. In Eq. (20) $\hat{\mathbf{s}}$ denotes the unit tangent vector along the interface. With the help of the generalized Darcy's law Eq. (3), we can say that

$$\mathbf{v}_1 = -\frac{b^2}{12\eta_1}\left[\nabla p_1 - \nabla\Psi - \frac{3\sigma_y(H)}{b}\hat{\mathbf{e}}_r\right] \tag{21}$$

and

$$\mathbf{v}_2 = -\frac{b^2}{12\eta_2}\nabla p_2. \tag{22}$$

Now subtract $\eta_2\mathbf{v}_2$ from $\eta_1\mathbf{v}_1$, evaluated at the interface, to obtain

$$\eta_2\mathbf{v}_2 - \eta_1\mathbf{v}_1 = -\frac{b^2}{12}\left[\nabla p_2 - \nabla p_1 + \nabla\Psi + \frac{3\sigma_y(H)}{b}\hat{\mathbf{e}}_r\right]. \tag{23}$$

This equation can be conveniently rewritten as

$$A\frac{(\mathbf{v}_1+\mathbf{v}_2)}{2} - \frac{(\mathbf{v}_1-\mathbf{v}_2)}{2} = \frac{b^2}{12(\eta_1+\eta_2)}\left\{\nabla\left[(p_1-p_2) - \Psi\right] - \frac{3\sigma_y(H)}{b}\hat{\mathbf{e}}_r\right\}. \tag{24}$$

Then, by taking the dot product of Eq. (24) with $\hat{\mathbf{s}}$ and writing the pressure difference $(p_1 - p_2)$ by using the pressure jump Eq. (6), we get

$$A\mathbf{V}\cdot\hat{\mathbf{s}} - \frac{\Gamma}{2} = -\frac{b^2}{12(\eta_1+\eta_2)} \times\left\{\nabla\left[\gamma\kappa + \frac{1}{2}\mu_0(\mathbf{M}\cdot\hat{\mathbf{n}})^2 + \Psi\right]\cdot\hat{\mathbf{s}} + \frac{3\sigma_y(H)}{b}\hat{\mathbf{e}}_r\cdot\hat{\mathbf{s}}\right\}, \tag{25}$$

In Eq. (25) $A = (\eta_2 - \eta_1)/(\eta_2 + \eta_1)$ is the viscosity contrast, and $\mathbf{V} = (\mathbf{v}_1 + \mathbf{v}_2)/2$ is an average velocity of the interface which can be expressed as a Birkhoff integral [56,57],

$$\mathbf{V}(s,t) = \frac{1}{2\pi}P\int ds'\frac{\hat{\mathbf{z}}\times[\mathbf{r}(s,t) - \mathbf{r}(s',t)]}{|\mathbf{r}(s,t) - \mathbf{r}(s',t)|^2}\Gamma(s',t), \tag{26}$$

where P means a principal-value integral and $\hat{\mathbf{z}}$ is the unit vector along the direction perpendicular to the cell. Finally, by explicitly writing the expressions for Ψ [Eq. (5)] and $\sigma_y(H)$ [Eq. (2)] in Eq. (25), a dimensionless equation for the vortex sheet strength can be obtained, yielding

$$\Gamma = 2\left\{A\mathbf{V}\cdot\hat{\mathbf{s}} + \nabla\left[\kappa + \frac{1}{2}\frac{N_B}{r^2}\chi[1+\chi(\hat{\mathbf{n}}\cdot\hat{\mathbf{e}}_\theta)^2] + S_0 r - \frac{S}{r}\right]\right\}\cdot\hat{\mathbf{s}}. \tag{27}$$

The term $(\hat{\mathbf{n}}\cdot\hat{\mathbf{e}}_\theta)^2$ in Eq. (27) is evocative of the magnetic normal traction contribution in Eq. (6). Notice that Eq. (27) is made dimensionless by using the same rescaling utilized to nondimensionalize Eqs. (8)–(13).

If one wishes to investigate the time evolution of the interface, one has to solve numerically a complicated nonlinear integrodifferential equation defined by (27) and (26). Nonetheless, a considerably simpler vorticity equation is obtained if one focus on the still fully nonlinear, but stationary, solutions

of Eq. (27). In this situation, we have that $\mathbf{v}_1 = \mathbf{v}_2 = 0$. By taking $\mathbf{V} = 0$ in Eq. (27), considering the condition of zero vorticity ($\Gamma = 0$), and writing $\hat{\mathbf{n}} \cdot \hat{\mathbf{e}}_\theta = r_s$, we find that

$$\kappa_s + \partial_s \left\{ \frac{1}{2} \frac{N_B}{r^2} \chi \left[1 + \chi r_s^2 \right] + S_0 r - \frac{S}{r} \right\} = 0, \qquad (28)$$

where the subscripts indicate derivative with respect to the arclength. Numerical solution of Eq. (28) is relatively simple [58–61] and offers a neat, nonperturbative way to access nontrivial, fully nonlinear, steady interfacial shapes in our problem. By integrating this differential equation, we readily find

$$\kappa = a - \frac{1}{2} \frac{N_B}{r^2} \chi \left[1 + \chi r_s^2 \right] - S_0 r + \frac{S}{r}, \qquad (29)$$

where a is a constant of integration.

Figure 4 depicts a representative set of nonperturbative, fully nonlinear stationary solutions acquired by the numerical integration of Eq. (28), taking into consideration the interfacial curvature expression (29). The resulting stationary shapes constitute N-fold symmetric structures, where the number of fingers depends on the physical parameters of the problem (N_B, χ, S, and S_0) and on the numerical constant a, which is related to the value of the curvature κ at $r = r_0$ [30,35,37,59]. We focus on the morphological features produced by the most prominent physical aspect of the MR fluid system: the magnetic field-dependent yield-stress parameter S. Therefore, in all patterns illustrated in Fig. 4 we take the typical values $N_B = 10$, $\chi = 1$, and $S_0 = 1$ as fixed parameters, as S is increased from the top to the bottom panel ($S = 2,5,10$).

Before we proceed, we make a few remarks about the unconstrained vortex sheet approach used to generate the shape solutions represented in Fig. 4. The shapes displayed in a given panel of Fig. 4 are obtained by utilizing the same physical parameters but can present different areas and contour lengths. In this framing, the different interfacial morphologies presented in a panel are obtained by varying a, which is arbitrary, and is carefully tuned in order to keep the interfacial curves commensurable and non-self-intercepting (see Refs. [30,35,37,58–61] for details). In other words, while we numerically search for physically relevant, closed, non-self-crossing interfacial patterns, we do it without imposing constraints on the area and perimeter of different patterned structures. This is the reason why one can observe that some patterns shown in Fig. 4 present different dimensions (enclosed area and boundary length). Nevertheless, these observations do not overshadow the most advantageous facet of the vortex sheet method: namely its ability to access essential, fully nonlinear elements of the patterns' morphologies. Finally, it should be emphasized that all patterns shown in Fig. 4 are a collection of stationary solutions and not a time-evolving sequence of events.

By inspecting Fig. 4, one notices that the morphology of the nonperturbative, fully nonlinear stationary solutions is consistent with the perturbative, weakly nonlinear, time-evolving patterned shapes presented in Sec. II B. Recall that our weakly nonlinear analysis predicted the development of structures presenting inward pointing fingers that should become wider at their tips as the parameter S is increased. This is in fact what is revealed in Fig. 4: as the value of S is increased from the top panel ($S = 2$) to the bottom panel ($S = 10$), the finger-widening effect becomes more pronounced due to the nonlinear action of the field-dependent yield stress, and the inward-pointing fingers of the MR fluid get flattened. One can also verify that the outward-pointing fingers of the nonmagnetic, inner fluid are comparatively narrower, tending to be more rounded (i.e., not flat) at their tips. This last feature is also in line with the predictions outlined in Sec. II B.

In addition to substantiating our weakly nonlinear findings, the vortex sheet approach unveils a morphological aspect that could not be foreseen at the weakly nonlinear regime: the occurrence of a finger pinch-off phenomenon. From Fig. 4 one observes that, as S is increased, the outward-pointing fingers of the inner fluid get "strangled" at their necks and tend to pinch off and eventually separate from the main body of the nonmagnetic bubble. It is worthwhile to note that similar pinch-off events have also been detected in other finite surface-tension Hele-Shaw flows (with nonmagnetic, as well as magnetic, fluids), notably those taking place in rotating Hele-Shaw cells [35,48,58,59].

Even though some of the stationary shapes we exemplified in Fig. 4 can be complicated, it is clear that they are still regular, showing some symmetry. We close this section by briefly commenting on the connection of these theoretical, stationary structures, with time-evolving shapes that eventually can arise in real experiments or numerical simulations. Under realistic experimental situations, one should expect the presence of noise during the time evolution of the interface. Possible sources of noise may come, for instance, from inhomogeneities on the plates of the Hele-Shaw cell, imperfections in the magnetic field arrangement, irregularities in the gap thickness b, or even from thermal or pressure fluctuations. Under such circumstances, the formation of unequal finger configurations presenting fingers that compete and present different lengths should be expected. Consequently, real experiments and numerical simulations can evolve towards configurations close to the stationary shape solutions depicted in Fig. 4 but probably presenting irregularities and asymmetries. They can also assume the shapes close to those illustrated in Fig. 4 during a transient but that eventually can depart from them.

Although the definite relevance of our current MR fluid steady shapes remains to be checked by experiments and advanced time simulations, there are existing evidence supporting the pertinence of such type of stationary solutions for other Hele-Shaw flow studies. This is particularly true for the Hele-Shaw problem in rotating cells involving nonmagnetic [48,53,58] or magnetic fluids [34,35]. For instance, the existence of symmetric stationary solutions in Refs. [53,58] can explain the experimental observation [48] of a plateau in the time evolution of the area of inner fluid contained in a reference circle. In addition, the stationary ferrofluid solutions obtained in Ref. [35] are found to be quite similar to the fully nonlinear, time-evolving patterns simulated numerically in Ref. [34]. Finally, in our present work, the morphological similarities between the time-evolving weakly nonlinear shapes shown in Fig. 3 and some of the stationary patterns depicted in Fig. 4 are also indicative that symmetric stationary solutions capture important qualitative features of the corresponding time-evolving shapes.

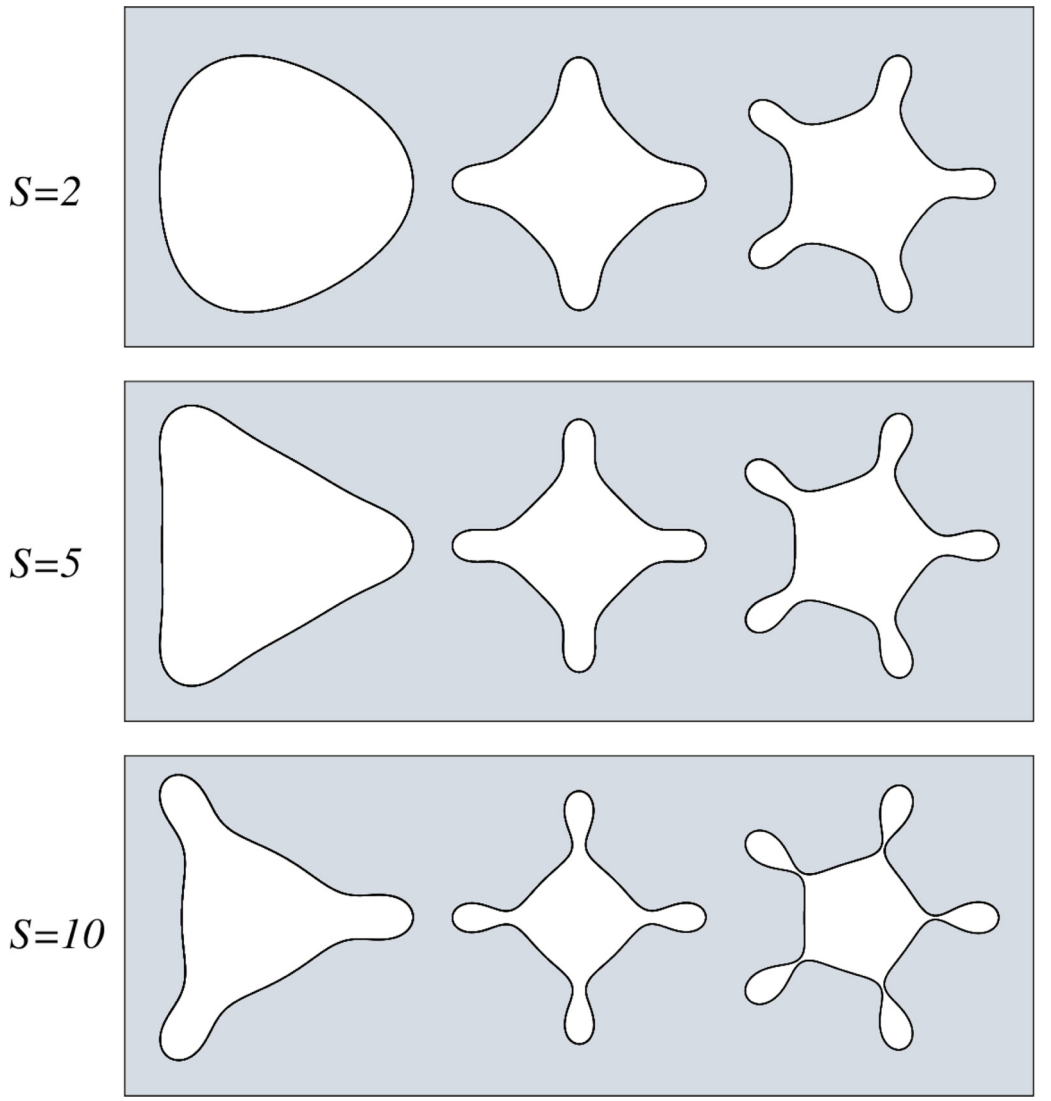

FIG. 4. (Color online) Typical nonperturbative, stationary shape solutions for a nonmagnetic fluid bubble surrounded by a MR fluid, considering three values of S. For each value of S the different N-fold patterns ($N = 3$, 4, and 5) are obtained by taking increasingly larger values of the constant of integration a (in a given panel a increases from left to right). The values we used for this constant of integration are as follows: top panel, $a = 5.881$, $a = 12.884$ and $a = 15.095$; middle panel, $a = 6.619$, $a = 11.149$, and $a = 12.290$; bottom panel, $a = 5.291$, $a = 6.609$, and $a = 6.860$.

IV. SUMMARY AND CONCLUSIONS

In contrast to what is observed in ferrofluid research, Hele-Shaw flow studies addressing interfacial pattern formation in MR fluids are relatively scarce in the literature. To contribute to the growth of this interesting, but still poorly explored, topic, in this work we have investigated the behavior of the interface separating a nonmagnetic inviscid bubble and a surrounding MR fluid when they are confined in a motionless Hele-Shaw cell. The fluid-fluid interface is made unstable through the action of an azimuthal magnetic field generated by a current-carrying wire. The wire is set perpendicularly to the Hele-Shaw cell plates and located at the center of the bubble. This magnetic field configuration produces a magnetic body force that acts radially inward, deforming the initially circular two-fluid interface. A conspicuous aspect of the problem is the fact that MR fluids present a dual solid-liquid behavior, characterized by a magnetic field-dependent yield stress. Another relevant physical ingredient of the system is surface tension: It tries to stabilize the deformed interface, tending to maintain it as close as possible to a circle. The interplay of magnetic, yield-stress, and surface tension forces ultimately determines the shape of the two-fluid interface.

Our study focuses on understanding the pattern-forming behavior of the interface during early linear, weakly nonlinear, and fully nonlinear regimes. Linear stability analysis reveals the destabilizing nature of the azimuthal magnetic field, as well as the stabilizing role played by surface tension and yield-stress contributions. On the other hand, mode-coupling analysis opens up the possibility of investigating analytically important morphological features of the evolving interface at the onset of nonlinear effects. In particular, we have found that, due to the action of the magnetic field-dependent yield stress, the resulting MR fluid patterns present inward pointing

fingers that have the tendency to become flat and wide at their tips. This morphological attribute has been confirmed by our fully nonlinear, nonperturbative vortex sheet results that unveiled the emergence of N-fold stationary structures having blunt inward-pointing fingers. We have also verified that these fingers are accompanied by the development of outward-pointing protuberances of the bubble, which eventually can lead to the occurrence of pinch-off events.

Our theoretical work makes specific predictions that have not yet been subjected to experimental check. We do hope that experimentalists, mainly those already working with magnetic fluids, will feel motivated to test our findings. On the theoretical side, a welcoming, natural extension of this work would be the investigation of fully nonlinear, time-evolving MR patterns via numerical simulations.

ACKNOWLEDGMENTS

J.A.M. thanks CNPq and FACEPE (through PRONEM Project No. APQ-1415-1.05/10) for financial support. E.O.D. acknowledges financial support from FACEPE through PPP Project No. APQ-0800-1.05/14.

APPENDIX: INFLUENCE OF THE DEMAGNETIZING FIELD

In this work we have considered only the lowest-order effect of the magnetic interactions that would result in fluid motion. Thus, in the azimuthal field situation, we have considered only the applied field in determining the magnetization. This is well justified by the fact that the azimuthal field is parallel to the plane of the Hele-Shaw cell, so the formation of magnetic surface charge densities that would have been responsible for inducing demagnetizing field effects is not favored [33,34,37]. For the sake of completeness, in this Appendix we extend our results by calculating the next order contribution on the interface dynamics due to the fringing field generated by induced magnetic charges in the perturbed circular droplet. This leading order correction appears at the linear growth rate and allows us to estimate the validity of the inductionless approximation.

We follow a procedure similar to the one presented in Ref. [62] by taking Eq. (3) and by considering that now the local magnetic field differs from the applied field $\mathbf{H}_0$ by a demagnetizing field of the polarized MR fluid $\mathbf{H} = \mathbf{H}_0 + \mathbf{H}_d$, where $\mathbf{H}_d = -\nabla\psi$ and ψ is the scalar magnetic potential,

$$\psi = \frac{1}{4\pi}\int_{\mathcal{S}} \frac{\mathbf{M}\cdot\mathbf{n}'}{|\mathbf{r}-\mathbf{r}'|}d^2r'. \tag{A1}$$

The unprimed coordinates $\mathbf{r}$ denote arbitrary points in space, and the primed coordinates $\mathbf{r}'$ are integration variables within the magnetic domain $\mathcal{S}$ defined on the ribbonlike interface separating the two fluids. The infinitesimal area element is denoted by $d^2r' = r'd\theta'dz'$. The vector

$$\mathbf{n}' = \frac{\left(\hat{\mathbf{e}}_r - \frac{1}{r'}\frac{\partial\zeta(\theta')}{\partial\theta'}\hat{\mathbf{e}}_\theta\right)}{\sqrt{1+\left(\frac{1}{r'}\frac{\partial\zeta(\theta')}{\partial\theta'}\right)^2}} \tag{A2}$$

represents the unit normal to the magnetic domain in consideration, bounded by $\mathcal{R}(\theta',t) = R + \zeta(\theta',t)$.

In order to determine ψ we take its first approximation as being the scalar magnetic potential related to the magnetic charges induced by the applied magnetic field. Therefore, the magnetization follows the linear relation $\mathbf{M} = \chi\mathbf{H_0} = \chi(I/2\pi r')\hat{\mathbf{e}}_\theta$. Taking this assumption into consideration, Eq. (A1) becomes

$$\psi = -\frac{\chi I}{8\pi^2}\int_{-b/2}^{+b/2}\int_0^{2\pi} \frac{\frac{1}{r'}\frac{\partial\zeta(\theta')}{\partial\theta'}}{\sqrt{1+\left(\frac{1}{r'}\frac{\partial\zeta(\theta')}{\partial\theta'}\right)^2}} \times \frac{d\theta'dz'}{\sqrt{r^2+r'^2-2rr'\cos(\theta'-\theta)+(z-z')^2}}. \tag{A3}$$

Regarding the magnetic-field-dependent yield stress, we point out that since the magnitude of the applied magnetic field is much larger than the magnitude of the demagnetizing field, in this analysis we may proceed considering $H \approx H_0$ in Eq. (2). It is also worth noticing that the corrections in the pressure jump condition (6) due to the demagnetizing field are of *third order* in ζ and, therefore, will not be present in our second-order approach.

By performing the linear perturbation analysis described in Sec. II A with the inclusion of the demagnetizing field, we derive a new expression for the linear growth rate:

$$\lambda(n) = |n|\left\{\frac{\chi N_B}{R^4}\left[1+\frac{2\chi}{\pi}W(n)\right] - \frac{(n^2-1)}{R^3} - \frac{S_0}{R} - \frac{S}{R^3}\right\}, \tag{A4}$$

where

$$W(n) = n\frac{R}{b}\int_0^{\pi/2}\left[\sqrt{1+\left(\frac{b\csc\tau}{2R}\right)^2}-1\right] \times \cos\tau\sin(2n\tau)d\tau. \tag{A5}$$

As we compare Eq. (A4) with Eq. (10), we notice that the term proportional to $W(n)$ is precisely the one related to the contribution of the demagnetizing field. By numerically integrating this extra demagnetizing term in the range of parameters we utilize in this work, we found that it corresponds to a maximum of 10% of the magnitude of the usual applied magnetic field term, and it does not lead to any qualitative difference in the growth rate behavior.

[1] J. Rabinow, Trans. Am. Inst. Elect. Eng. **67**, 1308 (1948).
[2] J. M. Ginder, in *Encyclopedia of Applied Physics*, edited by G. L. Trigg (VCH, Weinheim, 1996), Vol. 16, p. 487.
[3] J. M. Ginder, MRS Bull. **23**, 26 (1998).
[4] G. Bossis, S. Lacis, A. Meunier, and O. Volkova, J. Magn. Magn. Mater. **252**, 224 (2002).
[5] S. Genç and P. P. Phulé, Smart Mater. Struct. **11**, 140 (2002).
[6] H. A. Barnes, J. Non-Newtonian Fluid Mech. **81**, 133 (1999).

[7] D. Bonn and M. Denn, Science **324**, 1401 (2009).
[8] G. Ovarlez, Q. Barral, and P. Coussot, Nat. Mater. **9**, 115 (2010).
[9] P. Coussot, J. Non-Newtonian Fluid Mech. **211**, 31 (2014).
[10] R. Stanway, Mater. Sci. Technol. **20**, 931 (2004).
[11] J. de Vicente, D. J. Klingenberg, and R. Hidalgo-Alvarez, Soft Matter **7**, 3701 (2011).
[12] B. Park, F. Fang, and H. Choi, Soft Matter **6**, 5246 (2010).
[13] N. Umehara and K. Kato, J. Magn. Magn. Mat. **65**, 397 (1987).
[14] X. Zhu, X. Jing, and L. Cheng, J. Intell. Mater. Syst. Struct. **23**, 839 (2012).
[15] R. Ewoldt, G. McKinley, and A. Hosoi, Bull. Am. Phys. Soc. **53**, 252 (2008).
[16] S. A. Lira and J. A. Miranda, Phys. Rev. E **80**, 046313 (2009).
[17] R. H. Ewoldt, P. Tourkine, G. H. McKinley, and A. E. Hosoi, Phys. Fluids **23**, 073104 (2011).
[18] M. Lanzetta and K. Iagnemma, CIRP Ann. **62**, 21 (2013).
[19] M. Watanabe, N. Wiltsie, A. E. Hosoi, and K. Iagnemma, in *Proceedings of the 2013 IEEE/RSJ International Conference on Intelligent Robots and Systems (IROS), Nov. 2013* (IEEE, Piscataway, NJ, 2013), pp. 2315–2320.
[20] R. E. Rosensweig, *Ferrohydrodynamics* (Cambridge University Press, Cambridge, 1985).
[21] E. Blums, A. Cebers, and M. M. Maiorov, *Magnetic Fluids* (de Gruyter, New York, 1997).
[22] D. Andelman and R. E. Rosensweig, J. Phys. Chem. B **113**, 3785 (2009).
[23] H. Virpura, M. Parmar, and R. Patel, J. Nanofluid **3**, 121 (2014).
[24] For a recent review, see I. Torres-Díaz and C. Rinaldi, Soft Matter **10**, 8584 (2014).
[25] A. O. Tsebers and M. M. Maiorov, Magnetohydrodynamics (NY) **16**, 21 (1980).
[26] D. P. Jackson, R. E. Goldstein, and A. O. Cebers, Phys. Rev. E **50**, 298 (1994).
[27] F. Elias, C. Flament, J.-C. Bacri, and S. Neveu, J. Phys. I **7**, 711 (1997).
[28] C.-Y. Wen, C.-Y. Chen, and D.-C. Kuan, Phys. Fluids **19**, 084101 (2007).
[29] J. Kent-Dobias and A. J. Bernoff, Phys. Rev. E **91**, 032919 (2015).
[30] R. M. Oliveira, J. A. Miranda, and E. S. G. Leandro, Phys. Rev. E **77**, 016304 (2008).
[31] C.-Y. Chen, W.-L. Wu, and J. A. Miranda, Phys. Rev. E **82**, 056321 (2010).
[32] See, for instance, S. Elborai, D.-K. Kim, X. He, S.-H. Lee, S. Rhodes, and M. Zahn, J. Appl. Phys. **97**, 10Q303 (2005), and references therein.
[33] J. A. Miranda, Phys. Rev. E **62**, 2985 (2000).
[34] D. P. Jackson and J. A. Miranda, Phys. Rev. E **67**, 017301 (2003).
[35] S. A. Lira, J. A. Miranda, and R. M. Oliveira, Phys. Rev. E **82**, 036318 (2010).
[36] J. White, J. Oakley, M. Anderson, and R. Bonazza, Phys. Rev. E **81**, 026303 (2010).
[37] S. A. Lira, J. A. Miranda, and R. M. Oliveira, Phys. Rev. E **81**, 046303 (2010).
[38] E. O. Dias and J. A. Miranda, Phys. Rev. E **91**, 023020 (2015).
[39] J. A. Miranda and M. Widom, Physica D **120**, 315 (1998).
[40] G. H. Covey and B. R. Stanmore, J. Non-Newtonian Fluid Mech. **8**, 249 (1981).
[41] P. Coussot, J. Fluid Mech. **380**, 363 (1990).
[42] G. Homsy, Annu. Rev. Fluid Mech. **19**, 271 (1987); K. V. McCloud and J. V. Maher, Phys. Rep. **260**, 139 (1995); J. Casademunt, Chaos **14**, 809 (2004).
[43] P. Kuzhir, M. T. López-López, and G. Bossis, Phys. Fluids **21**, 053101 (2009).
[44] P. P. Phulé and J. M. Ginder, Int. J. Mod. Phys. B **13**, 2019 (1999).
[45] S. S. Deshmukh, Ph.D. thesis, Massachusetts Institute of Technology, 2007.
[46] P. Kuzhir, C. Magnet, L. Rodríguez-Arco, M. T. López-López, H. Fezai, A. Meunier, A. Zubarev, and G. Bossis, J. Rheol. **58**, 1829 (2014).
[47] E. Alvarez-Lacalle, E. Pauné, J. Casademunt, and J. Ortín, Phys. Rev. E **68**, 026308 (2003).
[48] E. Alvarez-Lacalle, J. Ortín, and J. Casademunt, Phys. Fluids **16**, 908 (2004).
[49] H. Gadêlha and J. A. Miranda, Phys. Rev. E **70**, 066308 (2004).
[50] A. Lindner, D. Derks, and M. J. Shelley, Phys. Fluids **17**, 072107 (2005).
[51] J. A. Miranda and E. Alvarez-Lacalle, Phys. Rev. E **72**, 026306 (2005).
[52] C.-Y. Chen, C.-H. Chen, and J. A. Miranda, Phys. Rev. E **73**, 046306 (2006).
[53] R. Folch, E. Alvarez-Lacalle, J. Ortín, and J. Casademunt, Phys. Rev. E **80**, 056305 (2009).
[54] R. Brandão, J. V. Fontana, and J. A. Miranda, Phys. Rev. E **90**, 053003 (2014).
[55] P. H. A. Anjos and J. A. Miranda, Soft Matter **10**, 7459 (2014).
[56] G. Tryggvason and H. Aref, J. Fluid Mech. **136**, 1 (1983).
[57] G. Birkhoff, Los Alamos Scientific Laboratory Technical Report No. LA-1862, 1954 (unpublished).
[58] E. Alvarez-Lacalle, J. Ortín, and J. Casademunt, Phys. Rev. Lett. **92**, 054501 (2004).
[59] E. S. G. Leandro, R. M. Oliveira, and J. A. Miranda, Physica D **237**, 652 (2008).
[60] G. Arreaga, R. Capovilla, C. Chryssomalakos, and J. Guven, Phys. Rev. E **65**, 031801 (2002).
[61] P. A. Djondjorov, V. M. Vassilev, and I. M. Mladenov, Int. J. Mech. Sci. **53**, 355 (2011).
[62] S. A. Lira and J. A. Miranda, Phys. Rev. E **86**, 056301 (2012).